

Fuzzy logic control of plug-in supercapacitor storage for thermoelectric management of batteries

Mukalu Sandro Masaki^{a,*}, Lijun Zhang^b, Xiaohua Xia^a

^a*Department of Electrical, Electronic and Computer Engineering, University of Pretoria, Pretoria 0002, South Africa*

^b*School of Artificial Intelligence and Automation, Huazhong University of Science and Technology, Wuhan 430072, China*

Abstract

Batteries are gaining momentum in the dawn of the global energy transition. Their propensity to early ageing remains, however, a serious concern. Reasons for this include thermal and electrical stresses experienced during operation. The combination of batteries with supercapacitors (SC) into hybrid energy storage systems (HESS) is currently regarded as an effective means of reducing electrical stress on batteries. However, battery-SC HESS still plays a marginal role in practice. Anticipating a possible resurgence of interest in this technology, controllers should be designed to enable easy conversion of existing battery energy storage systems (BESS) into battery-SC HESS. Currently, most control models in the literature would require significant modifications to the existing infrastructure, hindering the expected transition to the HESS. This paper introduces a fuzzy logic controller for plug-in SC aiming for straightforward conversion of BESS into battery-SC HESS. In addition to relieving batteries from fast-varying currents, the SC can contribute in the supply of slow-varying currents to further relieve the battery from electrical stresses and assist in regulating the battery temperature. Extensive simulations indicate that peak currents of batteries can be reduced by up to 26.20% under normal operation, and their temperature slope by up to 38.15% under high temperature conditions.

Keywords: hybrid energy storage system, battery, supercapacitor, fuzzy logic controller, thermal-electrical management.

1. Introduction

Energy storage systems are expected to play a critical role in our pursuit of a low-carbon economy and universal access to clean energy. While the global stationary and transportation energy storage market was estimated to be around 550 GWh in 2018, it is projected to increase fourfold by 2030 to more than 2,500 GWh [1]. Among the leading technologies is the battery characterized by high energy density, flexibility

*Corresponding author. Tel: +27 (0) 12 420 6767.

Email address: sdrmasaki@yahoo.fr (Mukalu Sandro Masaki)

and modularity [2, 3, 4]. This provides it with a competitive advantage in many applications, including transportation [5], off-grid and grid-tied renewable power systems [6, 7], and utility-scale energy storage for ancillary services [8]. While designed to operate between 10 and 15 years [9], batteries will usually suffer premature failure. Operational causes include high intensity, large current fluctuations, frequent charge-discharge transition, deep discharge, and thermal stress [10, 11]. Despite this, batteries are widely deployed as battery-alone energy storage systems (BESS). From a control point of view, these systems lack sufficient flexibility to effectively handle the degradation factors mentioned earlier.

1.1. Literature survey on battery-supercapacitor hybrid energy storage systems

The combination of batteries with one or more energy storage technologies to form battery-based hybrid energy storage systems (HESS) is today regarded as a promising solution to this shortcoming. In essence, an HESS relies on the beneficial coupling of two or more energy storage technologies with complementary operating features to outperform any single component of the system. Common battery-based HESS include battery-supercapacitors (SC), battery-fuel cell, battery-fuel cell-SC, battery-superconducting magnetic energy storage, battery-flywheel, and battery-compressed air storage [12]. Among them, the battery-SC association has recently gain in popularity driven by technical feasibility and maturity. When properly controlled, this superior storage system can feature high energy density, sustained by the battery, and fast power response and high power density, sustained by the supercapacitor. Methods for cost-effective sizing of this hybrid storage were previously proposed, including a capacity statistical model for autonomous microgrids [13], the tuning of the time constant of low-pass filter (LPF) for uninterrupted power supply applications [14] and utility scale PV arrays [15], and Particle Swarm Optimization for storage sizing in E-Rickshaw applications [16]. The positive impact of supercapacitor on the lithium battery cycle life in electric vehicle was also established in the past [17].

From a control perspective, various supervision algorithms for controlling the power allocation within the battery-SC HESS components are reported in the literature. The most basic and intuitive consists in applying a filter to assign the low and high frequency components of the input signal (power or current) respectively to the battery and the SC [18]. Without further actions, this method exposes the battery to deep discharge and overcharging risks. The utilization rate of SC might also be low, since there is no control action taken to maintain its state-of-charge (SoC) around a reference value. These concerns are usually addressed by more sophisticated protocols. [19] reported a fuzzy logic routine which, apart from the load current, considers the DC-bus voltage and the SC voltage to split power between the storage devices. A rule-based technique model that increases SC availability and limits the supply of large currents by the

battery was presented in [20]. The handling of high-frequency currents indistinctly by the battery and SC renders the last two models less effective.

A dynamic rate limiter that suppresses surges in battery current was reported in [21]. Optimal control for power allocation between battery and SC in HESS was also investigated in previous research [22, 23, 24]. A dynamic optimization model presented in [22] showed good power split capabilities in the context of battery-SC HESS operated as part of a grid-tied renewable power system. [23] proposed a two-layer receding horizon controller for maximum power supply by a hybrid renewable power system. In this study, the existing BESS is upgraded to a battery-SC HESS by adding SC, which results in smoother power profiles for the battery and the utility grid. An optimal power allocation strategy based on Pontryagin's minimum principle was proposed in [24]. The controller shows good performances in reducing battery power fluctuations and improving the utilization rate of supercapacitors. Soft computing techniques, such as artificial neural networks [25, 26] and fuzzy logic control [27, 28] were also considered for power allocation in battery-SC HESS. A Q-learning-based method to minimize battery degradation and energy consumption in battery/SC-powered electric vehicles was reported in [29].

In general, the above algorithms show good performance with respect to battery current fluctuations, charge-discharge transitions and deep discharge. However, they suffer from a few shortcomings. Firstly, the impact of high steady currents on batteries and the need to control them was usually overlooked, except in [28]. Secondly, the interaction between the power split problem and the regulation of the battery temperature was not considered in the past. Lastly, these control models entail relatively high levels of complexity and are computationally costly if fine control is to be maintained. While in 2014 the SC hit 4% of the global technology mix in energy storage deployments, this figure is now estimated to be less than 1% today [30, 31]. The tiny market share of SC suggests that the adoption of battery-SC HESS remains marginal in practice. In anticipation of a possible resurgence of interest in this technology, controllers of battery-SC HESS should preferably be designed to enable easy upgrade of existing battery-alone energy storage systems (BESS). As a result, the high complexity and computational cost of previous control models make them less suitable for direct retrofit of BESS, as a complete restructuring of the control infrastructure is necessary to ensure their smooth operation.

With respect to thermal management of batteries, their temperature should be regulated within a set range so as to ensure safety and an optimal trade-off between the operating performances and the storage service life. This ranges between 15°C and 35°C for lithium-ion batteries [32], and around 25°C for lead-acid batteries [33]. At lower temperatures, the two battery technologies exhibit sluggish chemistry, which results in temporary capacity loss, efficiency drop and reduced power and energy capabilities. On the other side,

the irreversible degradation of electrodes that occurs at higher temperatures causes accelerated ageing and capacity loss [34, 35, 36]. Battery cooling methods, such as air cooling, liquid cooling, direct refrigerant cooling, phase change material (PCM) cooling, thermoelectric cooling and heat pipe cooling [37, 38], are implemented to dissipate generated heat so as to prevent temperature rise. Air cooling can be natural or forced. The technologies that deliver high heat transfer efficiency are often complex and costly to operate [39]. On the other hand, Battery warm-up methods include internal heating via battery resistance, external heating via resistive heaters and circulated fluid [40].

A few studies on the operation of battery-SC HESS for battery thermal management were reported in the literature. A heuristic control strategy for battery cooling was presented in [41]. Under normal operations, the battery and SC are passively connected in parallel to supply the load. In case of high battery temperature, the two storage devices are alternatively connected and disconnected, resulting in the insertion of idle periods that slow down heat production in the battery without power supply interruptions. The lack of control over the SC in normal conditions hinders an effective power support to the battery. [42] proposed a receding horizon controller that simultaneously addresses the SoC and temperature imbalances between the battery modules and the energy losses in the converters that connect the battery and SC modules. While effective at improving temperature and energy distributions across the battery, the algorithm has little incidence on the regulation of the average battery temperature. A decrease in power support to the storage equipment is also noticed. [43] designed a controller that applies the pulse technique to reduce the average battery current during each pulse cycle. While this was expected to prevent the rise of battery temperature, failing to account for the actual need of the storage device can yield unnecessary cooling of batteries and workload for SC. With respect to battery heating, [36] proposed a heuristic model to minimize battery degradation and electricity costs in a battery-SC HESS powered electric vehicle operated at subzero temperatures. Here, the SC is primarily used to supply the peak load, while the baseload and the emergency situations are handled by the battery. To ensure proper operation under the targeted ambient conditions, i.e., between -20°C and 0°C , a heating resistor-fan kit serves to heat up the battery. The incidence of heat produced by the battery was not factored in the control of the heating system.

1.2. Literature gap and research contribution

The above survey of literature showed that the issue of power allocation within battery-SC HESS and that of battery thermal management are normally investigated separately, despite the well-known impact of high intensity currents on the latter. The few studies that attempted to take advantage of the power split operations for temperature regulation purposes failed to provide sufficient support to batteries either at the power [41] or thermal [43, 36, 28] level. Further, most reported controllers earlier are not suitable for easy

retrofit of existing BESS. In efforts to bridge this gap, the present study investigates a controller designed for thermal-electrical management of batteries within battery-SC HESS.

By means of a proper control of SC in the supply of high- and low-frequency currents, this controller relieves batteries from electrical stress and assists in the regulation of their temperature. In view of the penetration rate of BESS, the controller is designed for easy upgrade of BESS to battery-SC HESS. By requiring no modification in the existing control infrastructure, this plug-in solution safeguards from the extra technical, financial and environmental burdens related to the previous controllers that require shut-down, decommissioning, installation, recommissioning and possibly material disposal. These burdens might dissuade plant owners from upgrading existing BESS to battery-SC HESS.

The plug-in SC structure was introduced and studied in our previous work [23]. While delivering good performances, it was relevant only for grid-tied hybrid renewable systems equipped with BESS, and implementing a model predictive control. Moreover, battery thermal management was not considered in that study. The present work addresses these limitations. While gradient-based optimization algorithms have shown the greatest potential for real-time power management [44], the high computational cost and the difficulty of implementation make them less suitable for the retrofit application under study. This paper proposes a simple and low cost upgrade strategy built-around a fuzzy logic algorithm, which is less expensive in terms of computational time and memory. Successful applications of fuzzy logic controllers in power and transportation systems were reported in the literature [45, 46].

In summary, the novelty of this research is threefold:

1. It offers a unique low-cost solution for easy upgrade of BESS to battery-SC HESS without modifying the original infrastructure.
2. The issue of battery ageing due to high rate currents, previously overlooked, is addressed here.
3. The proposed power allocation strategy assists in the regulation of the battery temperature, which in turn decreases the loads of cooling and heating units.

Figure 1 shows the layout of the HESS under study. The original power system comprises a BESS, power sources, electric loads and relevant controllers to supervise the power flow across the system. The plug-in kit consists of a SC bank, a bidirectional DC/DC converter and an energy management system (EMS) that controls the power flow between the existing power system and the SC. Periodic measurements of the battery temperature and a number of electric variables are supplied the EMS. The battery temperature can be readily accessed from sensors that feed the temperature compensation circuit and/or the battery monitoring system.

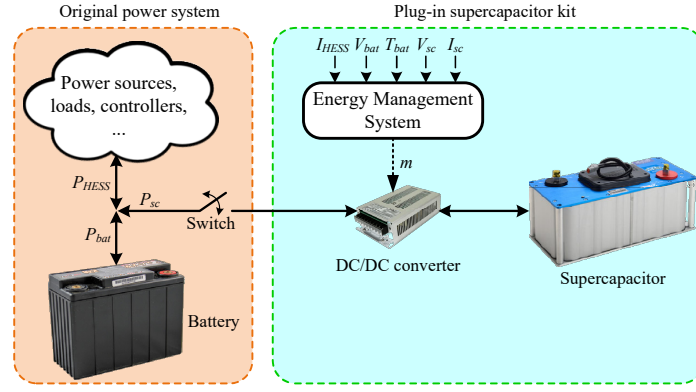


Figure 1: Layout of the battery-SC hybrid energy storage system

Besides the power split between the HESS components, the EMS also performs the following functions:

- Assist in keeping the battery temperature within the appropriate range;
- Maintain the SC state-of-charge (SoC) within the desired limits;
- Enable direct power flow between the battery and SC whenever necessary.

The rest of this paper is structured as follows. The design of the controller is carried out in Section 2. Section 3 introduces the optimization problem formulated for tuning the parameters of the fuzzy logic algorithm. Section 4 gives the case study considered for the test of the proposed controller. The presentation of simulation results and their discussion are provided in Section 5, followed by a brief conclusion in Section 6.

Nomenclature

Abbreviations and units

°C	Degree Celsius	A	Ampere
BESS	Battery-alone Energy Storage System	DC	Direct Current
EMS	Energy Management System	F	Farad
FIS	Fuzzy Inference System	GA	Genetic Algorithm
GWh	Gigawatt hour	H	Henry
HESS	Hybrid Energy Storage System	J	Joule
L	Low	LPF	Low-pass Filter
MF	Membership Function	NH	Negative High
NM	Negative Medium	PCM	Phase Change Material
PH	Positive High	PI	Proportional-Integral
PM	Positive Medium	PV	Photovoltaic

PWM	Pulse Width Modulation	p.u.	Per Unit
RMS	Root-mean-square	ROL	Rule Output Level
SC	Supercapacitor	S.I.	International System of Units
SoC	State-of-charge	V	Volts
W	Watt	Z	Zero
Ω	Ohm		
<i>Variables and parameters</i>			
C_{bat}	Battery thermal capacity (J/°C)	C_{fl}	Filter capacitance (F)
F_k	k-th Membership functions	i_{HESS}	Total current of HESS (p.u.)
i_{hf}	HESS' high-frequency current (p.u.)	i_{lf}	HESS' low-frequency current (p.u.)
I_{SC}	SC current (A)	$i_{sc,lf}$	SC's low-frequency current (p.u.)
$i_{sc,req}$	Required SC current (p.u.)	$I_{sc,req}$	Required SC current (A)
J	Fitness function	k_i	Integral gain
k_p	Proportional gain	L	Inductance value (H)
L_{fl}	Filter inductance (H)	m	Modulation index
N	Number of sample intervals	p	Laplace variable
P_{bat}	Battery heat generation (W)	R	Inductor resistance (Ω)
R_{b2a}	Thermal resistance battery-air (°C)/W	R_{bat}	Battery Ohmic resistance (Ω)
$I_{bat,nom}$	Battery nominal current (A)	R_{fl}	Filter resistance
SoC_{ref}	Reference SC's SoC	SoC_{sc}	SC SoC
$SoC_{sc,max}$	Maximum SC SoC	$SoC_{sc,min}$	Minimum SC SoC
t	Time (s)	T	Time constant of low-pass filter (s)
T_a	Ambient temperature (°C)	T_{bat}	Battery shell temperature (°C)
T_{max}	Maximum battery temperature (°C)	T_{ref}	Reference battery temperature (°C)
T_s	Sampling time (s)	v_k	Weighting coefficients
V_{bat}	Battery voltage (V)	V_L	Inductor voltage (V)
$V_{L,ref}$	Reference inductor voltage (V)	V_{SC}	SC voltage (V)
w_k	k-th rule firing strength	X	Array of optimized parameters
x_k	k-th parameters optimized by GA	z_k	k-th rule output levels

2. Controller design

Figure 2 shows the control system implemented by the EMS. It includes a low-pass filter (LPF), a FIS, a current controller and a few arithmetic operators. Once the plug-in kit is connected (switch in Fig. 1 is closed) and the required inputs are supplied to EMS, the following sequence of operations is periodically performed. Initially, the per-unit value i_{HESS} of the total current I_{HESS} requested from the HESS is filtered by the LPF to extract the low-frequency component, denoted by i_{lf} . A subtraction block determines the fast-varying, denoted by i_{hf} , from i_{HESS} and i_{lf} . i_{lf} is subsequently sent to the FIS that computes the slow-varying current $i_{sc,lf}$ to be handled by the SC. To assist in the thermal management of the battery and increase the utilization rate of SC, the battery shell temperature T_{bat} and the deviation of the supercapacitor state-of-charge SoC_{sc} from the desired level SoC_{ref} , denoted by ΔSoC_{sc} , are also supplied to FIS. The obtained value of $i_{sc,lf}$ is available at the output side of FIS. SoC_{ref} will typically be the midpoint between the lower and upper bounds of SoC_{sc} , denoted respectively by $SoC_{sc,min}$ and $SoC_{sc,max}$. Accordingly, ΔSoC_{sc} at a sample instant k is given by

$$\Delta SoC_{sc}(k) = SoC_{sc}(k) - SoC_{ref}, \quad (1)$$

with $SoC_{ref} = (SoC_{sc,min} + SoC_{sc,max})/2$. Next, i_{hf} and $i_{sc,lf}$ are summed up and converted back to SI unit to obtain the total current allocated to the SC, denoted by $I_{sc,req}$. This value is finally enforced by the current controller that requires the battery voltage V_{bat} , the SC voltage V_{sc} , and the SC current I_{sc} as additional input signals. The rest of this section focuses on the modelling of the controller components.

2.1. Frequency split of the HESS total current

Using the forward Euler method, the filtering action of LPF to extract i_{lf} from i_{HESS} is expressed by

$$i_{lf}(k+1) = \left(1 - \frac{T_s}{T}\right)i_{lf}(k) + \frac{T_s}{T}i_{HESS}(k), \quad (2)$$

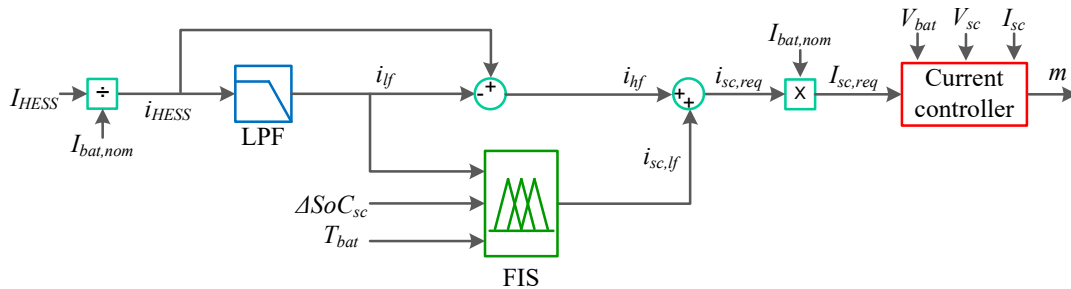


Figure 2: Proposed thermal-electrical controller for battery-SC HESS

with $i_{lf}(0) = i_{HESS}(0)$. Here, T_s and T denote the sample interval and the time constant respectively of the filter in seconds. Accordingly, the fast-varying current i_{hf} downstream the subtraction block is given by

$$i_{hf}(k+1) = i_{HESS}(k+1) - i_{lf}(k+1). \quad (3)$$

Given the fast change in polarity of i_{hf} and the use of $i_{sc,lf}$ to keep SoC_{sc} within the desired range through power exchange with the external power circuit and batteries, i_{hf} can be fully assigned to the SC.

2.2. Design of the fuzzy inference system

In mitigating the thermal stress and the high currents facing the battery, while maintaining SoC_{sc} within the desired limits, the FIS allocates on an ongoing basis a slow-varying current to SC considering its SoC, the battery temperature, and the magnitude and polarity of i_{lf} . Previous analysis of the performances of fuzzy systems showed that the precise shapes of membership functions (MFs) were of lesser importance than their number (partitions), their approximate placement across the universe of discourse (or universe), and the degree of overlapping of MFs [47]. Accordingly, the trapezoidal shape is selected for all the input MFs of FIS. In addition, the intuitive method is adopted to determine the number and placement of MFs, while Genetic Algorithm is used to optimize their overlapping and the parameters of output functions [47, 48]. Finally, the Sugeno fuzzy inference is implemented in FIS, because of its computational efficiency and effective tuning by optimization techniques [49].

Considering the impact of the intensity and polarity of i_{lf} on the HESS components, three MFs are assigned to i_{lf} : Negative High (NH), Low (L), and Positive High (PH), with L spreading on both sides of zero (no current). The polarities are such that NH and the negative portion of L correspond to charge current supplied to the HESS, while the positive portion of L and PH correspond discharge current request from the HESS. Given the need to maintain, as far as possible, SoC_{sc} around SoC_{ref} , three MFs are also assigned to the input variable ΔSoC_{sc} : Negative High (NH), Low (L) and Positive High (PH), with L spreading on both sides of the central value (zero deviation). Finally, previous experiments showed that the optimal operating temperature range for lithium-ion batteries was between 15 °C and 35 °C, while that of lead-acid batteries was around 25 °C [32, 33]. For both technologies, the universe of T_{bat} can be occupied by three MFs: Low (L), Medium (M) and High (H), with M spreading on both sides of the recommended temperature.

The governing principles in devising the fuzzy logic rules are as follows:

- (1) If T_{bat} is Medium then SC provides moderate support to the battery in supplying i_{lf} . This support varies with the intensity of i_{lf} and the deviation of SoC_{sc} from SoC_{ref} .

Table 0: Generalized fuzzy logic rules of FIS.

		i_{lf}		
		NH	L	PH
ΔSoC_{sc}	NH	$\alpha \cdot \text{NH}$	$\beta \cdot \text{NM}$	Z
	L	$\gamma \cdot \text{NM}$	Z	$\gamma \cdot \text{PM}$
	PH	Z	$\beta \cdot \text{PM}$	$\alpha \cdot \text{PH}$

- (2) If T_{bat} is Low then, taking “ T_{bat} is Medium” as reference operating condition, double the current flow from/to the battery. This results in halving the portion of i_{lf} assigned to the SC and doubling the current between SC and battery. No low-frequency current is however assigned to SC if ΔSoC_{sc} is Low.
- (3) If T_{bat} is High then, taking “ T_{bat} is Medium” as reference operating condition, reduce by half the current flow from/to the battery. This results in doubling the portion of i_{lf} assigned to the SC and halving the current between SC and battery.

A general formulation of the fuzzy logic rules of FIS is provided in Tables 0. The rule output levels (ROs) of FIS are defined as follows: NH for negative high, NM for negative medium, Z for zero, PM for positive medium, and PH for positive high. Given the governing principles introduced earlier, the parameters α , β and γ are such that:

- $\alpha=0.5$, $\beta=2$ and $\gamma=0$ if T_{bat} is Low;
- $\alpha=1$, $\beta=1$ and $\gamma=1$ if T_{bat} is Medium;
- $\alpha=2$, $\beta=0.5$ and $\gamma=2$ if T_{bat} is High;

Details on the formulation of ROs as functions of input variables is presented later in Section 3.

2.3. Current controller

Figure 3 shows the PI current controller, adapted from [50], together with the power circuit that connects the SC in parallel with the battery. Here, L and R denote respectively an inductor and its equivalent series resistance. Based on the average model of the DC/DC converter, the plant to be controlled in the SC current control loop is given by Eqs. (4) and (5)

$$V_{sc} - V_L = mV_{batt}, \quad (4)$$

$$V_L = RI_{sc} + L \frac{dI_{sc}}{dt}, \quad (5)$$

where V_L denotes the terminal voltage across the inductor. If the inductor voltage is adopted as the control variable, then the plant to be controlled is described by the Laplace transformation of (5) as follows

$$I_{sc}(p) = \frac{1}{Lp + R}V_L(p), \quad (6)$$

where p is the Laplace transform variable. Based on (4), the modulation index m is therefore obtained as follows

$$m = \frac{V_{sc} - V_{L,ref}}{V_{bat}}, \quad (7)$$

where $V_{L,ref}$ denotes the PI controller output [50]. The corresponding block diagram of the current controller is shown in Fig. 3. In this diagram, $I_{sc,req}$ is divided by the modulation index m so that the reference SC current is transferred from the battery side to the SC side of the DC/DC converter. $V_{L,ref}$ is given in Laplace domain by

$$V_{L,ref}(p) = \left(k_p + \frac{k_i}{p}\right)E(p), \quad (8)$$

where k_p and k_i denote respectively the proportional gain and the integral gain of the PI controller, and $E(p)$ denotes the Laplace transform of the error signal expressed by

$$E(p) = I_{sc,req}^*(p) - I_{sc}(p). \quad (9)$$

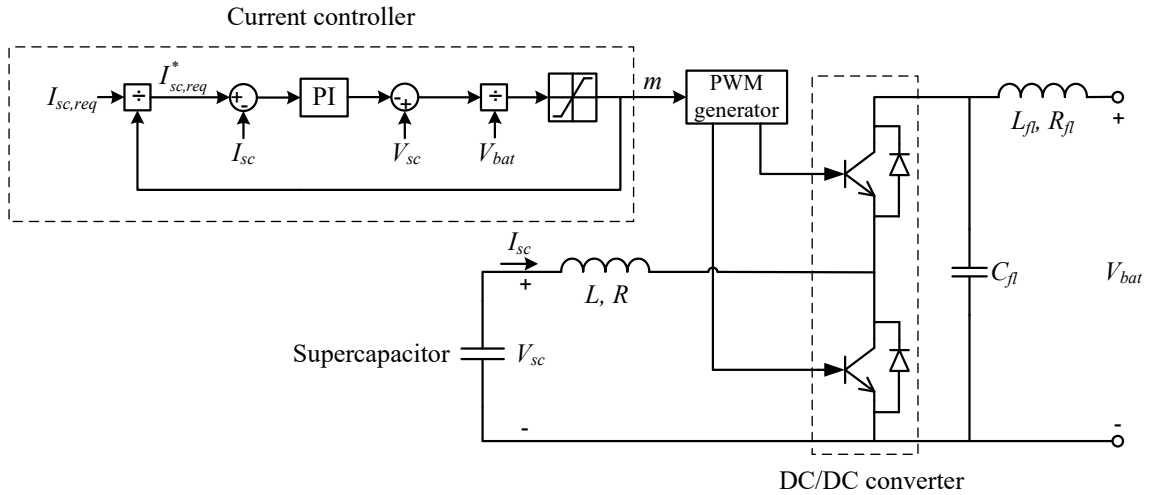
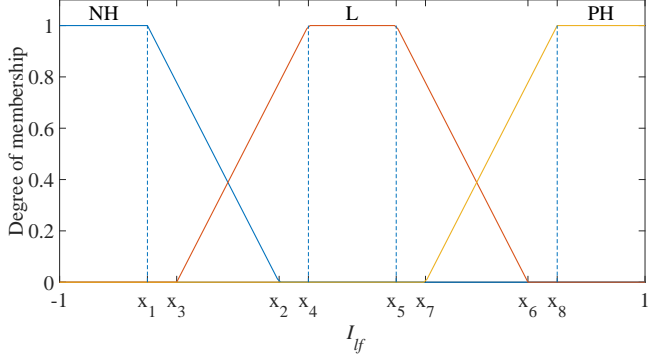
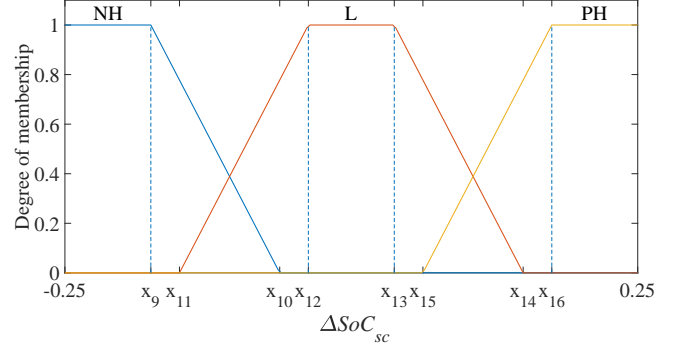


Figure 3: Current controller and power circuit of SC



(a) Slow-varying component of I_{HESS} , i_{if}



(b) Deviation of the state-of-charge of SC

Figure 4: Parameters of the input membership functions optimized by GA

3. Genetic Algorithm-based optimization of FIS parameters

3.1. Overview of Genetic Algorithms

Genetic algorithms are a population-based optimization technique inspired by both the natural selection theory and the evolutionary genetics [51, 52]. To evolve an initial population of individuals (candidate solutions) towards the optimal one within a search space, three basic operations are repeatedly applied by genetic algorithms to form the next generation from the current population:

- Selection: choose individuals (parents) that survive the current population to contribute to the next generation.
- Crossover: combine pairs of parents to form new individuals (children) for the next generation.
- Mutation: apply random alterations (mutations) to individual parents to create children.

In this respect, the individuals are compared to each other using their respective fitness values obtained by evaluating the function to be optimized (fitness function). Typically, parents with better fitness values are more likely to be selected by genetic algorithms. Interested readers may refer to [52, 53] for further information on genetic algorithms.

3.2. Optimization model

This section introduces the optimization problem solved by Genetic Algorithm to obtain the parameters of FIS.

3.2.1. Optimization variables and FIS output

The array X optimized by Genetic Algorithm includes the parameters of input MFs and those of ROLs. Figure 4 shows the MF parameters of input variables optimized by GA. It is noteworthy that the MF

parameters of T_{bat} are derived from previous experiments, and are therefore not subject to optimization. Based on the governing principles identified in Section 2.2, the rule output levels of FIS can be generalised as follows:

$$z_k = \lambda_k(x_j i_{lf} + x_{j+1} \Delta SoC_{sc}), \quad (10)$$

where z_k ($k = 1, \dots, 27$) denotes a ROL in Table 0, $\lambda_k \in \Lambda = \{0, 0.5, 1, 2\}$, and x_j and x_{j+1} are parameters optimized by GA, with j denotes the element index in the array X . Table 0 shows that the determination of ROLs NH, NM, Z, PM and PH under medium T_{bat} , i.e. $\alpha = \beta = \gamma = 1$, is sufficient to obtain the ROLs under low and high T_{bat} . Accordingly, the rest of analysis of Table 0 in this section relates to medium battery temperature conditions, unless stipulated otherwise.

The formulation of NH, NM, Z, PM and PH as functions of the optimization variables is carried out here. Table 0 shows that the charge of SC under the ROL NH depends closely on the supply of a high intensity current i_{lf} by the external circuit. Similarly, the discharge of SC under the ROL PH is primarily performed by supplying an intensive current i_{lf} to the external circuit. Given the high intensity of i_{lf} , the component proportional to ΔSoC_{sc} in Eq. (10) is redundant, and may cause excessive current transients across the HESS. Accordingly, the parameters x_{j+1} in Eq. (10) are set at zero for both NH and PH. In the case of the ROL Z, x_j and x_{j+1} are equal to zero so that no slow-varying current is allocated to the SC. Finally, Table 0 shows that the ROL NM applies to “low ΔSoC_{sc} /negative high i_{lf} ” and “negative high ΔSoC_{sc} /low i_{lf} ” conditions. Similarly, the ROL PM applies to “low ΔSoC_{sc} /positive high i_{lf} ” and “positive high ΔSoC_{sc} /low i_{lf} ” conditions. Therefore, the first term in the brackets of Eq. (10) should dominate the output when i_{lf} is of high intensity, while the second term should dominate when ΔSoC_{sc} is high. Accordingly, both x_k and x_{k+1} are required for both NM and PM.

Equations (11) to (15) summarize the above findings:

$$\text{NH} = x_{17} i_{lf}, \quad (11)$$

$$\text{NM} = x_{18} i_{lf} + x_{19} \Delta SoC_{sc}, \quad (12)$$

$$\text{Z} = 0, \quad (13)$$

$$\text{PM} = x_{20} i_{lf} + x_{21} \Delta SoC_{sc}, \quad (14)$$

$$\text{PH} = x_{22} i_{lf}, \quad (15)$$

where x_{17}, \dots, x_{22} are the ROL parameters optimized by GA.

Considering Eq. (10), the final output $i_{sc,lf}$ of FIS is determined as follows

$$i_{sc,lf} = \frac{\sum_{k=1}^N w_k z_k}{\sum_{k=1}^N w_k}, \quad (16)$$

where $N=27$ is the total number of rules, w_k denotes the rule firing strength derived from the rule antecedent, and is given by

$$w_k = \min(F_1(i_{lf}), F_2(\Delta SoC_{sc}), F_3(T_{bat})). \quad (17)$$

Here, $F_1(\dots)$, $F_2(\dots)$ and $F_3(\dots)$ are the membership functions for inputs 1, 2, and 3, respectively, and \min denotes the mathematical function “minimum” that implements the fuzzy logical operator AND.

3.2.2. Fitness function

In this study, the fitness function $J(X)$ is formulated to minimize the thermal and electrical stress on the battery, while maximizing the availability of SC. Accordingly, $J(X)$ is formulated as a multi-objective objective function consisting of three factors:

- (1) the root-mean-square (RMS) current of the battery [14], denoted by $J_1(X)$.
- (2) the mean deviation of the battery temperature from the recommended value, denoted by $J_2(X)$.
- (3) the mean absolute deviation of SoC_{sc} from SoC_{ref} , denoted by $J_3(X)$.

The fitness function minimized by GA is therefore given by

$$J(X) = v_1 J_1(X) + v_2 J_2(X) + v_3 J_3(X), \quad (18)$$

where v_1 to v_3 are weighting coefficients, and $X = [x_1, x_2, \dots, x_{22}]^T$ corresponds to the array of optimization variables identified earlier.

Let N denote the number of sample intervals within the optimization period, the normalized expression of J_1 is given by

$$J_1(X) = \frac{1}{I_{bat,nom}} \sqrt{\frac{1}{N} \sum_{k=1}^N I_{bat,k}^2(X)}, \quad (19)$$

where $I_{bat,k}(X)$ denotes the battery current during the k -th sample interval.

The normalized expression of J_2 is given by

$$J_2(X) = \frac{1}{N(T_{max} - T_{ref})} \sum_{k=1}^N |T_{bat,k}(X) - T_{ref}|, \quad (20)$$

where T_{max} and T_{ref} denote the maximum attainable and the recommended temperatures respectively.

The normalized expression of J_3 is given by

$$J_3(X) = \frac{1}{N\Delta SoC_{sc,max}} \sum_{k=1}^N |\Delta SoC_{sc,k}(X)|, \quad (21)$$

where $\Delta SoC_{sc,max}$ denotes the maximum deviation of SoC_{sc} from SoC_{ref} , and $\Delta SoC_{sc,j}$ is given by

$$\Delta SoC_{sc}(k) = SoC_{sc}(k) - SoC_{ref}. \quad (22)$$

Here, $SoC_{sc}(k)$ is obtained using the Coulomb counting approach as follows:

$$SoC_{sc}(k) = SoC_{sc}(k-1) + \frac{I_{sc}(k)}{CV_{max}} T_s, \quad (23)$$

where $I_{sc}(k)$ corresponds to the SC current during the sample time k , C is the capacitance of the SC in Farads, and V_{max} is the maximum voltage of the SC in Volts.

Considering the lumped RC-thermal circuit model of the battery, its thermal behaviour is modelled as

$$P_{bat} = C_{bat} \frac{dT_{bat}}{dt} + \frac{T_{bat} - T_a}{R_{b2a}}, \quad (24)$$

where P_{bat} , T_{bat} , T_a , C_{bat} , and R_{b2a} denote the battery heat generation, battery temperature, ambient temperature, thermal capacity of the battery, and thermal resistance between battery and ambient air, respectively.

Because the ohmic heat varies proportionally to the square of the current, it will usually form the primary source of heat generation inside the battery under large load current. The battery heat generation can be therefore modelled as

$$P_{bat} = R_{bat} I_{bat}^2, \quad (25)$$

where R_{bat} denotes the ohmic resistance of the battery. Substituting (25) into (24) yields after discretization

$$T_{bat}(k) = \left(1 - \frac{T_s}{C_{bat} R_{b2a}}\right) T_{bat}(k-1) + \frac{T_s}{C_{bat}} \left(R_{bat} I_{bat}^2(k) + \frac{T_{amb}}{R_{b2a}}\right). \quad (26)$$

3.2.3. Optimization constraints

The following constraints retain the trapezoidal shape of membership functions in Fig. 4(a), and ensure that the overlaps are confined along their oblique sides:

$$x_1 - x_2 \leq 0 \quad (27)$$

$$x_1 - x_3 \leq 0, \quad (28)$$

$$-x_2 + x_3 \leq 0, \quad (29)$$

$$x_2 - x_4 \leq 0, \quad (30)$$

$$x_3 - x_4 \leq 0, \quad (31)$$

$$x_4 - x_5 \leq 0, \quad (32)$$

$$x_5 - x_6 \leq 0, \quad (33)$$

$$x_5 - x_7 \leq 0, \quad (34)$$

$$-x_6 + x_7 \leq 0, \quad (35)$$

$$x_6 - x_8 \leq 0, \quad (36)$$

$$x_7 - x_8 \leq 0, \quad (37)$$

Similarly, the following constraints retain the trapezoidal shape of membership functions in Fig. 4(b), and ensure that the overlaps are confined along their oblique sides:

$$x_8 - x_{10} \leq 0 \quad (38)$$

$$x_9 - x_{11} \leq 0, \quad (39)$$

$$-x_{10} + x_{11} \leq 0, \quad (40)$$

$$x_{10} - x_{12} \leq 0, \quad (41)$$

$$x_{11} - x_{12} \leq 0, \quad (42)$$

$$x_{12} - x_{13} \leq 0, \quad (43)$$

$$x_{13} - x_{14} \leq 0, \quad (44)$$

$$x_{13} - x_{15} \leq 0, \quad (45)$$

$$-x_{14} + x_{15} \leq 0, \quad (46)$$

$$x_{14} - x_{16} \leq 0, \quad (47)$$

$$x_{15} - x_{16} \leq 0, \quad (48)$$

The constraint (49) ensures that the SC is directly charged by the battery when i_{lf} and ΔSoC_{sc} are respectively L and NH:

$$x_5 x_{18} + x_9 x_{19} \leq 0. \quad (49)$$

The following constraint is introduced to guarantee the charging of SC when i_{lf} and ΔSoC_{sc} are respectively NH and L:

$$x_1x_{18} + x_{13}x_{19} \leq 0. \quad (50)$$

The constraint (51) ensures that the SC get discharged when i_{lf} and ΔSoC_{sc} are respectively L and PH:

$$-x_4x_{20} - x_{16}x_{21} \leq 0. \quad (51)$$

The following constraint is introduced to guarantee the discharging of SC when i_{lf} and ΔSoC_{sc} are respectively PH and L:

$$-x_8x_{20} - x_{12}x_{21} \leq 0. \quad (52)$$

Considering the fuzzy rules in Table 0, the constraints (53) and (54) ensure that the peak of the ROL NH is inferior to that of NM.

$$x_1x_{17} - x_4x_{18} - x_9x_{19} \leq 0. \quad (53)$$

$$x_1x_{17} - x_1x_{18} - x_{12}x_{19} \leq 0. \quad (54)$$

Similarly, the constraints (55) and (56) ensure that the peak of the ROL PH is superior to that of PM.

$$x_8x_{20} + x_{13}x_{21} - x_8x_{22} \leq 0. \quad (55)$$

$$x_5x_{20} + x_{16}x_{21} - x_8x_{22} \leq 0. \quad (56)$$

The bound limits are as follows

$$-1 \leq x_1, x_2, x_3, x_4 \leq 0. \quad (57)$$

$$0 \leq x_5, x_6, x_7, x_8 \leq 1. \quad (58)$$

$$\Delta SoC_{sc,min} \leq x_9, x_{10}, x_{11}, x_{12} \leq \Delta SoC_{sc,avg}. \quad (59)$$

$$\Delta SoC_{sc,avg} \leq x_{13}, x_{14}, x_{15}, x_{16} \leq \Delta SoC_{sc,max}. \quad (60)$$

$$1/4 \leq x_{17}, x_{19}, x_{21}, x_{22} \leq 1/2. \quad (61)$$

Algorithm 1: Evaluation of individual fitness in Genetic Algorithm

```

1 Build FIS using  $X$ , Fig. 4, Table 0, and Eqs. (11) to (15);
2 for  $k = 1$  to  $N$  do
3   Determine  $i_{lf}(k)$  and  $i_{hf}(k)$  from  $i_{HESS}$ , Eq. (2) and Eq. (3);
4   Compute  $i_{lf,sc}(k)$  from FIS, with  $i_{lf}(k)$ ,  $\Delta SoC_{sc}(k)$  and  $T_{bat}(k)$  as inputs ;
5    $I_{sc,req}(k) \leftarrow (i_{hf}(k) + i_{sc,lf}(k))I_{bat,nom}$  ;
6    $I_{sc}(k) \leftarrow I_{sc,req}(k)$  ;
7    $I_{bat}(k) \leftarrow I_{HESS}(k) - I_{sc}(k)$  ;
8   Determine  $T_{bat}(k+1)$  from Eq. (26), and  $\Delta SoC_{sc}(k+1)$  from Eqs. (22) and (23);
9 end
10 Determine  $J_1(X)$ ,  $J_2(X)$  and  $J_3(X)$  from Eqs (19), (20) and (21), respectively;
11  $J(X) \leftarrow v_1J_1(X) + v_2J_2(X) + v_3J_3(X)$ .

```

$$0 \leq x_{18}, x_{20} \leq 1/4. \quad (62)$$

The boundaries (61) on x_{17} and x_{22} result in a relatively large current assigned to the SC if i_{lf} is of high intensity. Similarly, the bound limits on x_{19} , x_{21} result in a relatively large current assigned to the SC if ΔSoC_{sc} is high. In both cases, the current supplied by the SC does not exceed $\frac{1}{2}I_{bat,nom}$ so that the rules α -NH and α -PH in Table 0 under low battery temperature, and β -NM and β -PM in Table 0 under high battery temperature do not cause the slow-varying current $i_{sc,lf}$ to exceed 1, or $I_{bat,nom}$ in physical unit. The boundaries (62) applied to x_{18} and x_{20} require the SC to handle a relatively small portion of $i_{sc,lf}$ when it is medium, i.e, under NM and PM rules.

3.2.4. Optimization problem

Considering the above, the optimization problem solved by GA is summarized as follows:

$$\begin{aligned}
& \min_X J(X) \\
& \text{s.t. } G(X) \leq 0,
\end{aligned}$$

where J is detailed by inequalities (18), (19) and (21), and $G(X)$ consists of equations (27) through to (62). Algorithm 1 describes the steps in determining the fitness value of an individual, i.e, a candidate solution X to the optimization problem.

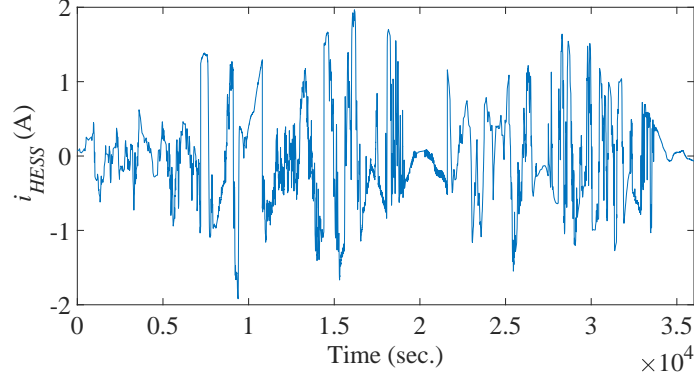


Figure 5: Sandia National Laboratory’s load profile for determination of duty cycle for energy storage systems in a PV smoothing application

4. Case study

An HESS consisted of four 3.6V lithium-ion battery cells and twelve 2.7V supercapacitor cells is considered in this simulation study. Details on the characteristics of storage devices are depicted in Table 1. To ensure a stable operation of the retrofitted HESS and to prolong the SC lifespan, the variation of SoC_{sc} is restricted between 0.5 and 1. The following scenarios that correspond to normal and extreme operating conditions are considered to test the controller:

- Scenario I — Optimal conditions: T_{amb} and $T_{bat}(0)$ are both set at 25 °C, $SoC_{sc}(0)$ is set around 75 %, and i_{HESS} has a non-zero profile.
- Scenario II.a — Low temperature mode: T_{amb} and $T_{bat}(0)$ are both set at 5 °C, $SoC_{sc}(0)$ is set around 75 %, and i_{HESS} has a non-zero profile.
- Scenario II.b — High temperature mode: T_{amb} and $T_{bat}(0)$ are both set at 45 °C, $SoC_{sc}(0)$ is set around 75 %, and i_{HESS} has a non-zero profile.

Put together, these scenario provide a full picture of the expected performances of the controller, should it be used under the recommended conditions or far away from the appropriate temperature range.

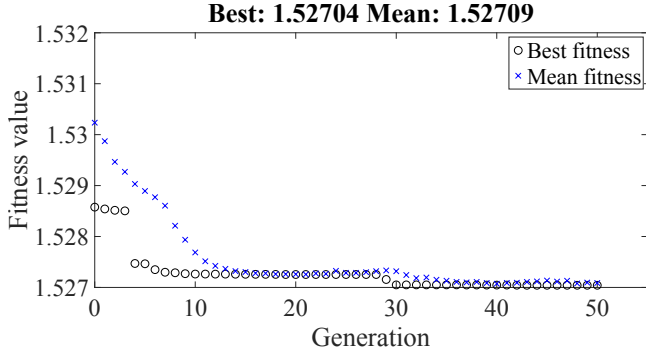
5. Simulations and discussion

5.1. Controller parameters

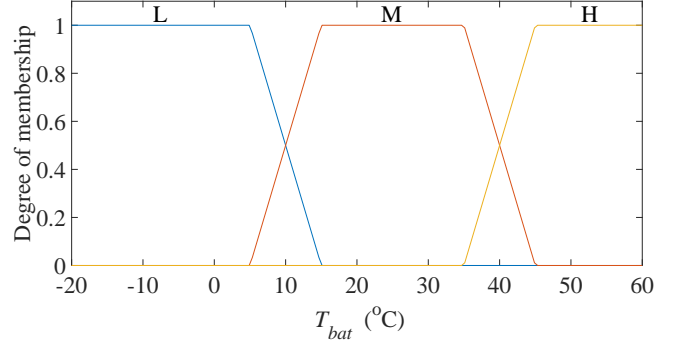
Figure 5 presents the load profile obtained from the U.S. guideline for determination of duty cycle for energy storage systems in a PV smoothing application [56]. This load profile I_{HESS} was applied to the battery-SC HESS to compute the optimal array X of controller parameters. In the rest of this paper, the sign convention is such that a negative current always flows towards the storage device to charge it. Fig.

Table 1: Simulation parameters for testing of the battery-SC HESS controller

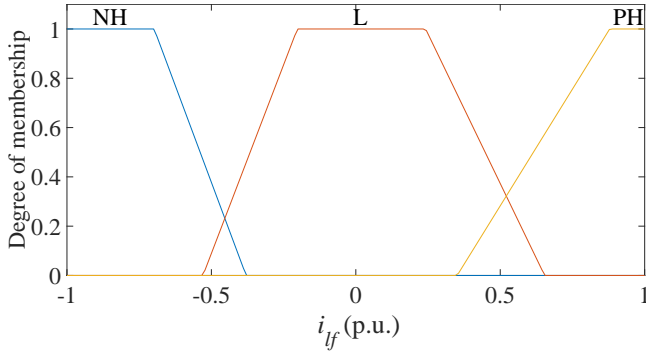
Parameter	Value	Unit	Parameter	Value	Unit
Battery cells [41, 54]			GA parameters		
$E_{batt,nom}$	8.64	Wh	$v_1; v_2; v_3$	0.25; 0.25; 0.5	
$V_{batt,nom}$	3.60	V	Population size	100	
$I_{batt,nom}$	2.20	A	Elite count	5	%
R_{batt}	0.10	Ω	Crossover fraction	0.8	
$C_{batt,cell}$	17.26	J/ $^{\circ}$ C	Low-pass filter		
$R_{b2a,cell}$	6.84	$^{\circ}$ C/W	T	100	sec.
# in series	4		Current controller		
Supercapacitor cells [55]			k_p	1.85	
$C_{sc,nom}$	450.00	F	k_i	2720	
$V_{sc,nom}$	2.70	V	DC-DC converter		
$R_{sc,cell}$	2.80e-3	Ω	L, L_{fl}	0.56	mH
$R_{b2a,cell}$	6.84	$^{\circ}$ C/W	R, R_{fl}	0.09	Ω
# in series	6		C_{fl}	72.73	mF
# in parallel	2		Switching frequency	20	kHz



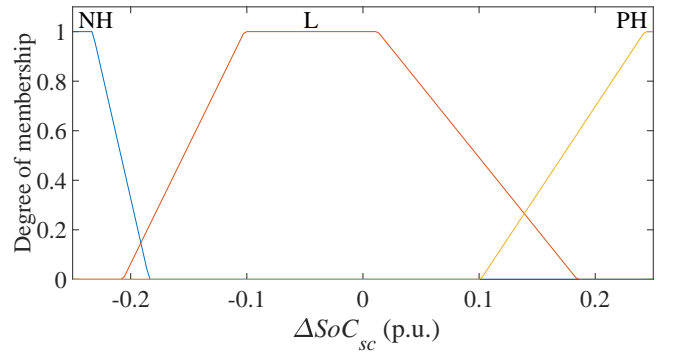
(a) Convergence curve of Genetic Algorithm



(b) Membership functions of T_{bat} for Li-ion batteries



(c) Membership functions of i_{lf}



(d) Membership functions of ΔSoC_{sc}

Figure 6: Optimization outputs from Genetic Algorithm

6(a) shows the convergence curve obtained for the case study introduced earlier subject to the load profile in Figure 5. Figure 6(b) shows the MFs of T_{bat} derived from previous experiments on lithium-ion batteries [32]. The optimized array X of controller parameters is as follows: $X = [-0.6981; -0.3797; -0.5292; -0.2025; 0.2417; 0.6537; 0.3508; 0.8789; -0.2328; -0.1841; -0.2067; -0.1020; 0.0127; 0.1845; 0.1014; 0.2427; 0.3896; 0.2054; 0.3053; 0.1785; 0.3317; 0.3600]$. The membership functions of i_{lf} and ΔSoC_{sc} are shown in Fig. 6(c) and Fig. 6(d), respectively.

5.2. Scenario I: Controller performance under normal operating conditions

The battery-supercapacitor HESS and the proposed controller were implemented in Simulink/Matlab. Figure 7 presents the current profiles under a fast-varying load, with both the ambient and initial battery temperature set at 25°C. Here, the subscript w/o corresponds to the performance obtained when the SC is controlled by the LPF alone, while w refers to the performance under full implementation of the proposed EMS. It shows that the presence of LPF causes the SC to handle the spiky content of I_{HESS} . As a result, the current supplied by the battery within the LPF-controlled HESS (Fig. 7(b)) is smoother than that of the BESS (Fig. 7(a)). Fig. 7(c) shows the current profile of the SC, which shows fast fluctuations. Under full deployment of the EMS, the FIS limits the supply of high intensity current by the battery. This is

achieved by diverting part of low-frequency content of I_{HESS} towards the SC, as depicted in Fig. 7(d). Under normal operating conditions, the SC contributes up to 18.28% in the supply of low-frequency current by the HESS. In comparison to BESS and HESS,w/o alternatives, Table 2 shows that the RMS value of the battery current (J_1) decreases by, respectively, 26.20% and 13.77% under the new controller. Moderate improvement on the deviations of battery temperature (J_2) and SC SoC (J_3) from specified values is also noticed.

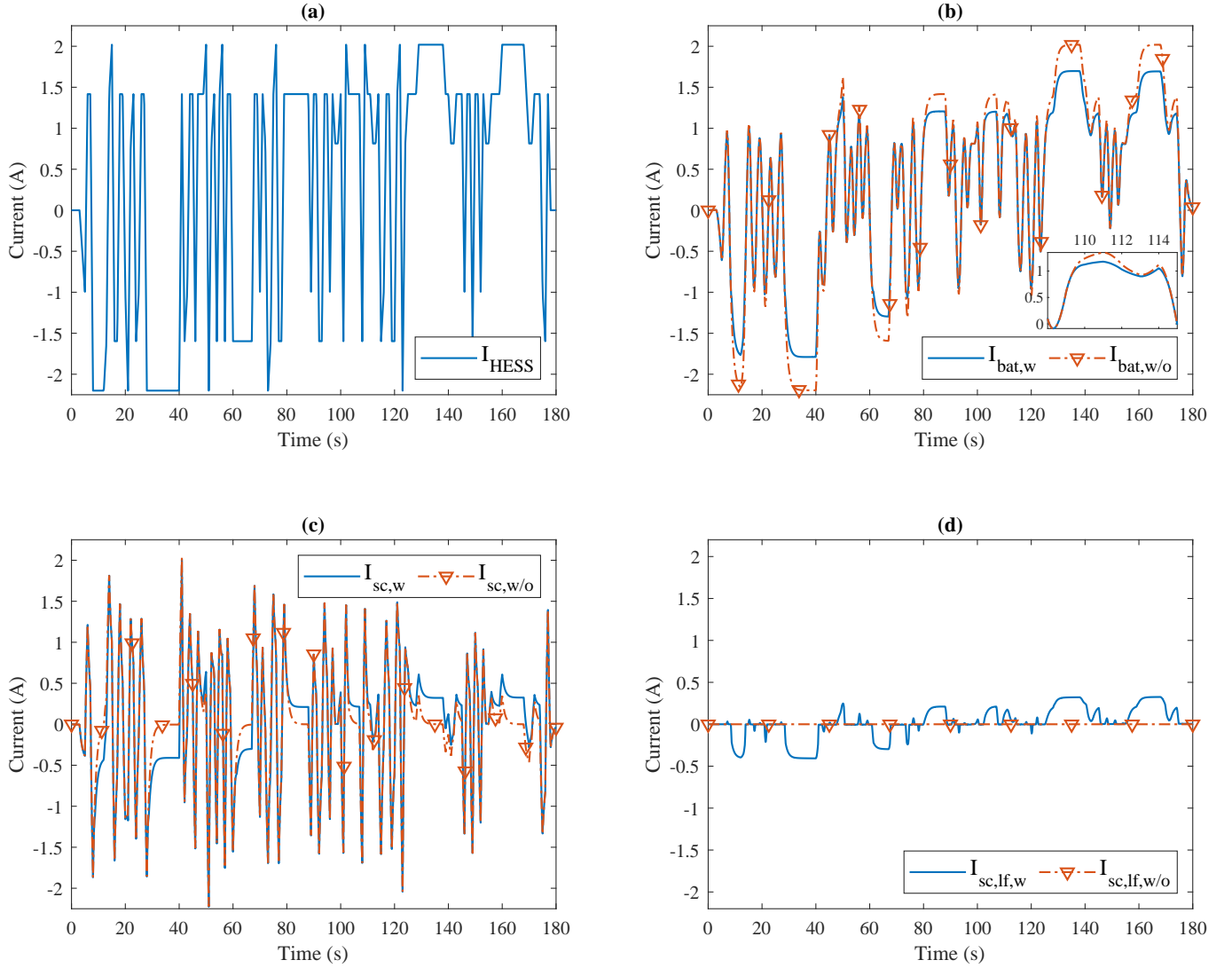


Figure 7: Current profiles under a fast-varying load. (a) Total current requested from the HESS. (b) Battery current. (c) SC current. (d) Low-frequency content of SC current.

Figure 8 plots the evolution of battery temperature, assuming that the current profiles given in 7(a) and (b) repeat continuously for six hours.

Based on previous studies on the cyclic ageing of batteries [57, 58], the capacity loss is given by Eq. 63 :

$$Q_{bat,loss} = B(C) \exp\left(\frac{-31700 + 370.3C}{RT_{bat}}\right) (A_h)^z, \quad (63)$$

Table 2: Performance indexes under normal and critical operating modes

Simulation	J_1			J_2			J_3		
	BESS	HESS,w/o	HESS,w	BESS	HESS,w/o	HESS,w	BESS	HESS,w/o	HESS,w
Scenario 1	0.6398	0.5476	0.4722	0.0018	0.0014	0.0012	-	0.0062	0.0050
Scenario 2.a	0.8854	0.7099	0.8796	0.5665	0.5674	0.5665	-	0.0215	0.0002
Scenario 2.b	0.8854	0.7099	0.5405	0.5773	0.5762	0.5751	-	0.0140	0.0336

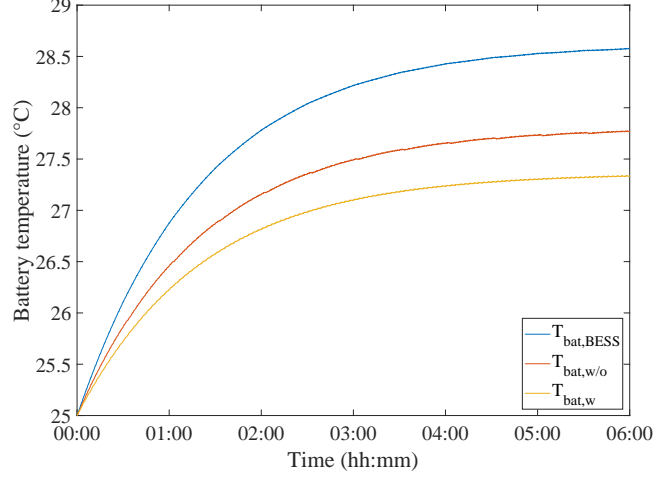


Figure 8: Evolution of battery temperature under scenario I

with

$$B = 25623.71C^{-0.28}. \quad (64)$$

Here, B denotes the pre-exponential factor; C denotes the C-rate; R stands for the ideal gas constant, which is equal to $8.314 \text{ J}(\text{kg K})^{-1}$; T_{bat} denotes the absolute battery shell temperature in K; A_h denotes the Ah throughput of the battery; z stands for the power law coefficient, which is equal to 0.552. In this study, A_h corresponds to the product of $I_{bat,RMS}$ and the total time of operation. To determine the battery lifetime, it is assumed to operated for six hours, as shown in Fig. 8, and is rested for 18 hours daily. The end of life is reached when the battery loses 20% of its nominal capacity given in Table 1.

For each configuration, Table 3 shows the RMS current of the battery ($I_{bat,RMS}$), the final temperature ($T_{bat,SS}$), the average temperature ($T_{bat,avg}$), the total battery capacity loss $Q_{bat,loss}$ over the same period, and the corresponding theoretical battery lifespan. It appears that the proposed plug-in module increases the theoretical lifespan of the battery by 17.00% and 7.75% compared, respectively, to the BESS and the HESS controlled by the filter alone.

Table 3: Assessment of theoretical battery ageing

	$I_{bat,RMS}$ (A)	$T_{bat,SS}$ (°C)	$T_{bat,avg}$ (°C)	$Q_{bat,loss}$ (%)	Lifespan (hours)
BESS	1.408	28.623	27.803	0.330	60.575
HESS,w/o	1.200	27.802	27.174	0.304	65.777
HESS,w	1.004	27.361	26.833	0.282	70.872

5.3. Scenario II: Controller performance under extreme ambient temperatures

5.3.1. Scenario II.a: Supercapacitor support under low temperature conditions

The effectiveness of the battery-SC HESS controller in low temperature environment is investigated in this section. A scenario that assumes the storage system functioning in room temperature at 5 °C is considered to evaluate the performances under extremely cold operating conditions. Figure 9 depicts the current and temperature profiles in the battery-SC HESS in this context. Here, the subscripts w and wo denote respectively the performances obtained by considering and ignoring the battery temperature in the control strategy. The latter is evaluated by maintaining the fuzzy input T_{bat} constantly at the reference value of 25 °C.

In operating the battery-SC HESS in cold environment to supply the load shown in Fig. 9(a), the controller that involves the battery temperature tends to increase the battery current (cf. Fig. 9(b)) by decreasing the portion of low-frequency current assigned to SC (cf. Fig. 9(c)). This results in increased battery heating by Joule’s effect (cf. Fig. 9(d)), causing faster rise of temperature so as to move it near the optimal range. Except for the handling of fast transitions by SC, the profiles of battery current and temperature are identical to those observed under the BESS. In comparison to BESS and HESS,w/o alternatives, Table 2 shows that the average deviation of the battery temperature (J_2) decreases, respectively, by 0% and 0.15% over the six minutes of functioning under the new controller. The latter is accompanied by 23.82% increase in the RMS value of I_{bat} (J_1), because battery warming receives higher priority. A significant improvement of 99.07% is also reported on the deviation of SC SoC.

5.3.2. Scenario II.b: Supercapacitor support under high temperature conditions

The effectiveness of the battery-SC HESS controller in high temperature environment is investigated in this section. A scenario that assumes the hybrid storage system functioning at a room temperature of 45 °C is proposed to evaluate the performance under extremely hot operating conditions. Figure 10 shows the various current and temperature profiles under the different configurations.

When operating the battery-SC HESS under high ambient temperature to supply the load in Fig. 10(a),

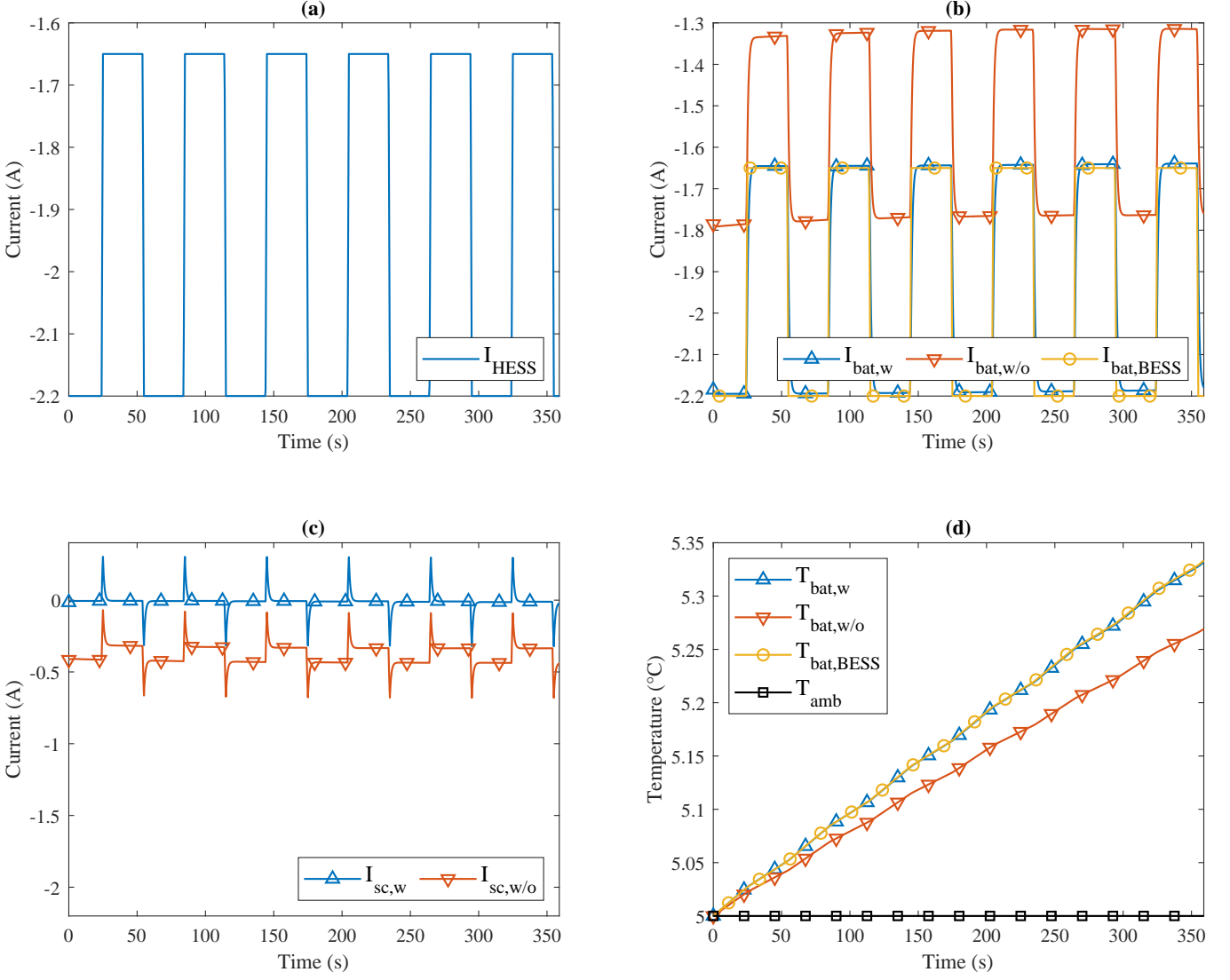


Figure 9: Current and temperature profiles under room temperature at 5 °C

the controller supplied with the battery temperature in input tends to reduce its current (cf. Fig. 10(b)) by increasing the low-frequency current assigned to SC (cf. Fig. 10(c)). This reduces battery heating by Joule's effect, slowing the temperature rise. Compared to the BESS, Figure 10(d) shows that 38.15% decrease in the battery temperature slope is achieved by the new controller. Further, Table 2 reports, after functioning six minutes, 0.3% and 0.19% decrease in battery temperature deviation (J_2) compared respectively to BESS and *w/o* alternatives. This is accompanied by 38.95% and 23.87% decrease in the RMS value of I_{bat} (J_1). A degradation of 140% is also reported on the deviation of SC SoC.

6. Conclusions and future work

This paper has presented a fuzzy logic controller for plug-in supercapacitor modules thoughtfully designed for easy upgrade of battery-alone storage systems to battery-supercapacitor HESS. Through an adequate

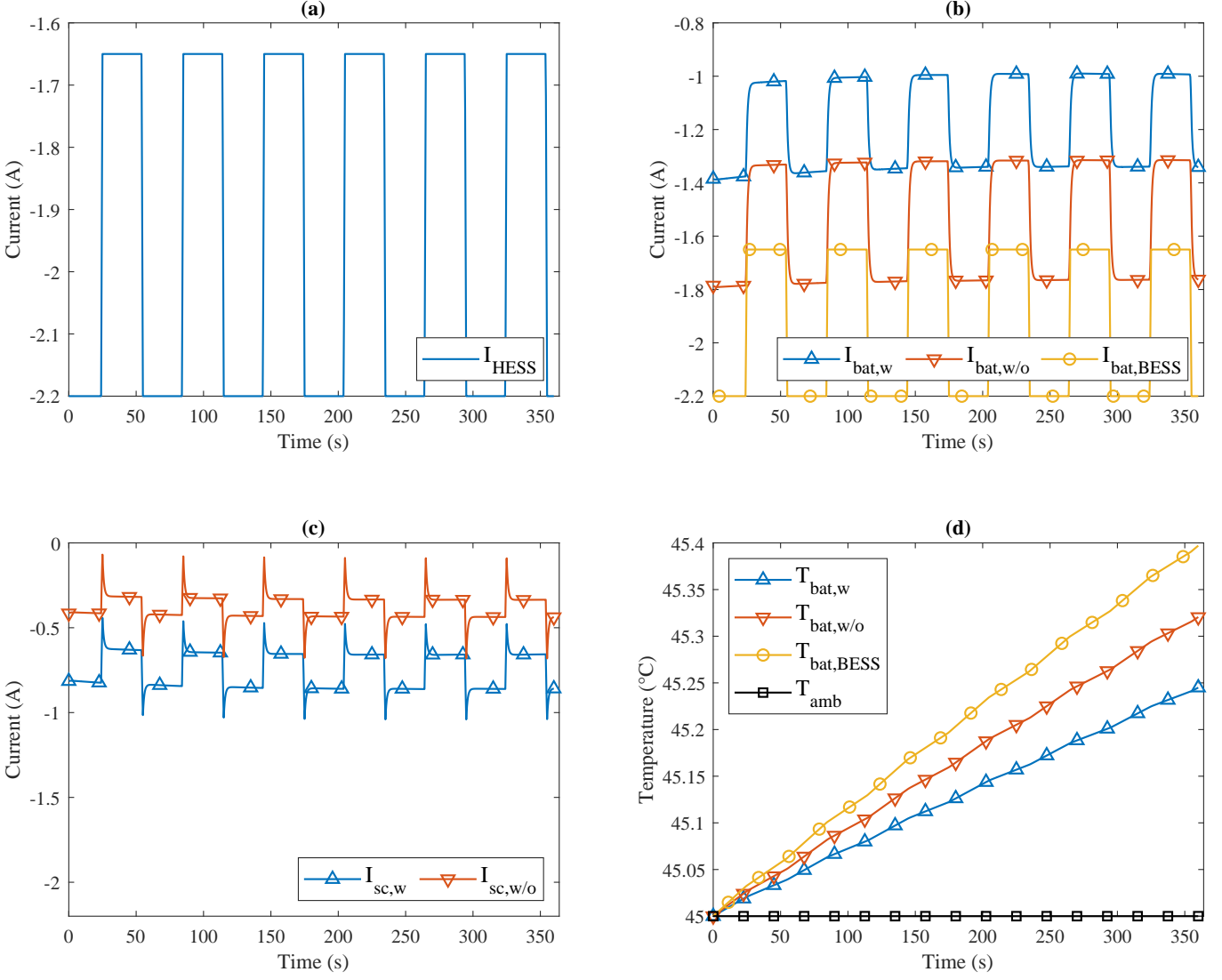


Figure 10: Current and temperature profiles under ambient temperature at 45 °C

control of supercapacitors that contribute in the supply of both high and low frequency currents, the proposed EMS mitigates the electric and thermal stresses on batteries, resulting in extended lifespan. The simulation study showed that up to 26.20% decrease in peak battery current can be achieved under normal ambient conditions, and up to 38.15% decrease in battery temperature slope can be achieved under high temperature conditions. Moreover, The thermal support from the SC is gradually decreased when battery warm-up increase in priority. The proposed controller showed better performance than the battery-alone storage systems. It also outperforms the previous battery-supercapacitor HESS controllers with respect to ease of implementation and extent of support to batteries.

While the proposed EMS has proved to be effective in extending the lifespan of batteries, future research is needed to further inform the decision-making process. One area of future work is in devising a suitable approach for sizing the supercapacitors and DC/DC converter so that the economic benefit at the plant

level is maximized. This can offer a solid ground to help the management decide whether to upgrade his/her BESS or not.

Appendix A. Block diagram simulation model of the battery-supercapacitor HESS

The power and control layers of the model implemented Matlab/Simulink block are shown in Figure A.1 and Figure A.2 respectively.

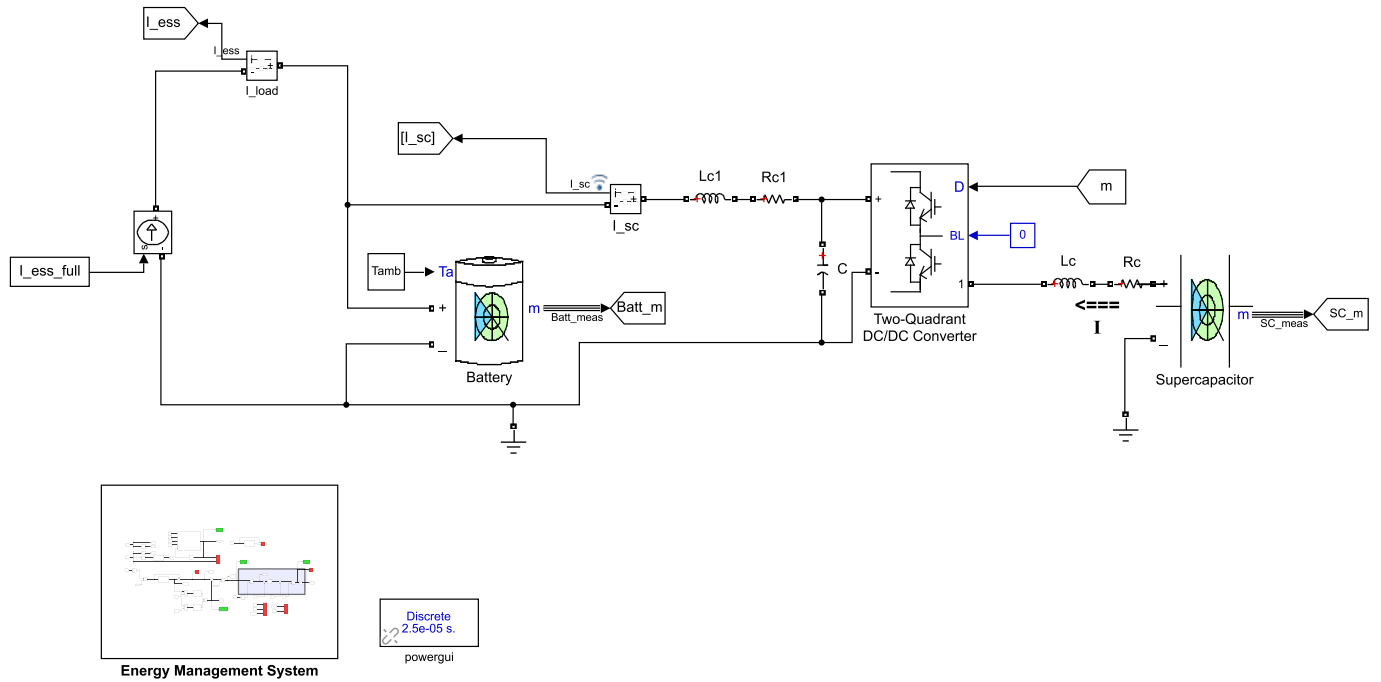


Figure A.1: Power layer of the block diagram in Simulink

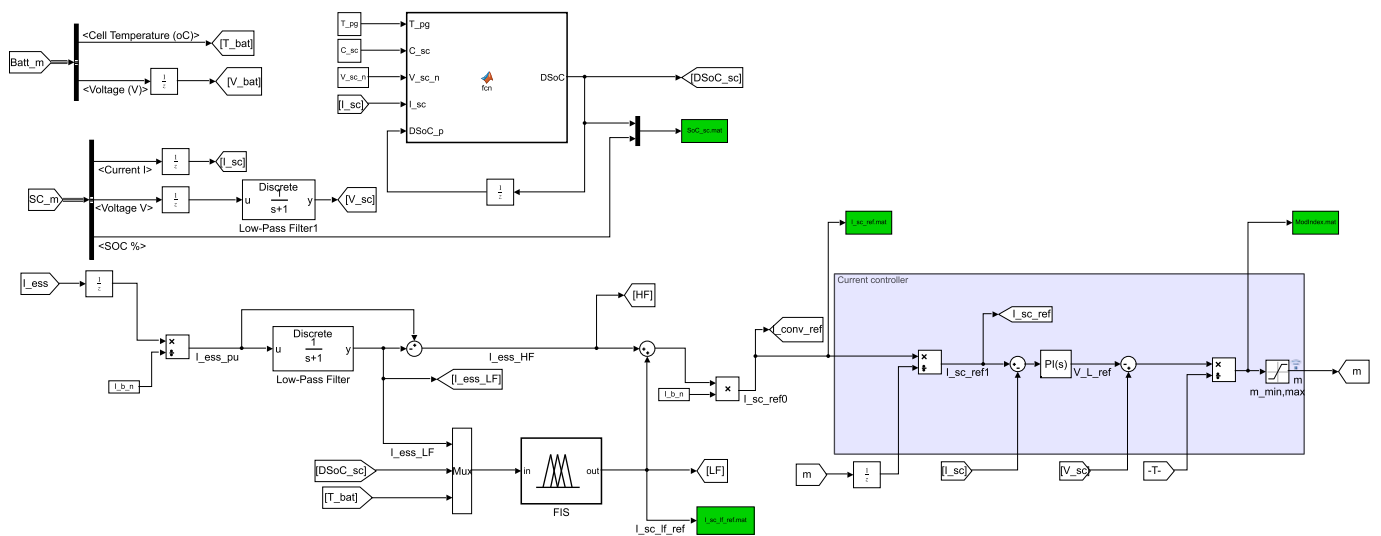


Figure A.2: Energy Management System (control layer) in Simulink

References

- [1] U.S. Department of Energy, Energy storage grand challenge: Energy storage market report (December 2020).
URL https://www.energy.gov/sites/prod/files/2020/12/f81/Energy%20Storage%20Market%20Report%202020_0.pdf
- [2] G. L. Soloveichik, Battery technologies for large-scale stationary energy storage, *Annual Review of Chemical and Biomolecular Engineering* 2 (2011) 503–527.
- [3] J. Chang, J. Shang, Y. Sun, L. K. Ono, D. Wang, Z. Ma, Q. Huang, D. Chen, G. Liu, Y. Cui, et al., Flexible and stable high-energy lithium-sulfur full batteries with only 100% oversized lithium, *Nature Communications* 9 (1) (2018) 1–11.
- [4] F. Nadeem, S. S. Hussain, P. K. Tiwari, A. K. Goswami, T. S. Ustun, Comparative review of energy storage systems, their roles, and impacts on future power systems, *IEEE Access* 7 (2018) 4555–4585.
- [5] K. Turcheniuk, D. Bondarev, G. G. Amatucci, G. Yushin, Battery materials for low-cost electric transportation, *Materials Today* 42 (2020) 57–72.
- [6] P. Ortega-Arriaga, O. Babacan, J. Nelson, A. Gambhir, Grid versus off-grid electricity access options: A review on the economic and environmental impacts, *Renewable and Sustainable Energy Reviews* 143 (2021) 110864.
- [7] N. Kittner, F. Lill, D. M. Kammen, Energy storage deployment and innovation for the clean energy transition, *Nature Energy* 2 (9) (2017) 17125.
- [8] A. Kumar, N. K. Meena, A. R. Singh, Y. Deng, X. He, R. Bansal, P. Kumar, Strategic integration of battery energy storage systems with the provision of distributed ancillary services in active distribution systems, *Applied Energy* 253 (2019) 113503.
- [9] P. Haidl, A. Buchroithner, B. Schweighofer, M. Bader, H. Wegleiter, Lifetime analysis of energy storage systems for sustainable transportation, *Sustainability* 11 (23) (2019) 6731.
- [10] M. R. Palacín, A. de Guibert, Why do batteries fail?, *Science* 351 (6273) (2016) 1253292.
- [11] N. Harting, R. Schenkendorf, N. Wolff, U. Krewer, State-of-health identification of lithium-ion batteries based on nonlinear frequency response analysis: First steps with machine learning, *Applied Sciences* 8 (5) (2018) 821.
- [12] S. Hajiaghahi, A. Salemnia, M. Hamzeh, Hybrid energy storage system for microgrids applications: A review, *Journal of Energy Storage* 21 (2019) 543–570.
- [13] H. Jia, Y. Mu, Y. Qi, A statistical model to determine the capacity of battery–supercapacitor hybrid energy storage system in autonomous microgrid, *International Journal of Electrical Power & Energy Systems* 54 (2014) 516–524.
- [14] A. Lahyani, A. Sari, I. Lahbib, P. Venet, Optimal hybridization and amortized cost study of battery/supercapacitors system under pulsed loads, *Journal of Energy Storage* 6 (2016) 222–231.
- [15] P. K. S. Roy, H. B. Karayaka, Y. Yan, Y. Alqudah, Investigations into best cost battery-supercapacitor hybrid energy storage system for a utility scale pv array, *Journal of Energy Storage* 22 (2019) 50–59.
- [16] S. Bansal, P. Nambisan, M. Khanra, Optimal sizing and cost analysis of battery/supercapacitor alone and in combination for e-rickshaw application, in: 2019 Fifth Indian Control Conference (ICC), IEEE, 2019, pp. 500–505.
- [17] N. Vukajlović, D. Milićević, B. Dumnić, B. Popadić, Comparative analysis of the supercapacitor influence on lithium battery cycle life in electric vehicle energy storage, *Journal of Energy Storage* 31 (2020) 101603.
- [18] W. Jing, C. H. Lai, D. K. Ling, W. S. Wong, M. D. Wong, Battery lifetime enhancement via smart hybrid energy storage plug-in module in standalone photovoltaic power system, *Journal of Energy Storage* 21 (2019) 586–598.
- [19] M. Sellali, S. Abdeddaim, A. Betka, A. Djerdir, S. Drid, M. Tiar, Fuzzy-super twisting control implementation of battery/super capacitor for electric vehicles, *ISA transactions* 95 (2019) 243–253.

- [20] Z. Bai, Z. Yan, X. Wu, J. Xu, B. Cao, H control for battery/supercapacitor hybrid energy storage system used in electric vehicles, *International Journal of Automotive Technology* 20 (6) (2019) 1287–1296.
- [21] A. Parwal, M. Fregelius, I. Temiz, M. Götteman, J. G. de Oliveira, C. Boström, M. Leijon, Energy management for a grid-connected wave energy park through a hybrid energy storage system, *Applied Energy* 231 (2018) 399–411.
- [22] M. S. Masaki, L. Zhang, X. Xia, Hierarchical power flow control of a grid-tied photovoltaic plant using a battery-supercapacitor energy storage system, *Energy Procedia* 145 (2018) 32–37.
- [23] M. S. Masaki, L. Zhang, X. Xia, A hierarchical predictive control for supercapacitor-retrofitted grid-connected hybrid renewable systems, *Applied Energy* 242 (2019) 393–402.
- [24] J. He, C. Shi, T. Wei, X. Peng, Y. Guan, Hierarchical optimal energy management strategy of hybrid energy storage considering uncertainty for a 100% clean energy town, *Journal of Energy Storage* 41 (2021) 102917.
- [25] J. Faria, J. Pombo, M. d. R. Calado, S. Mariano, Power management control strategy based on artificial neural networks for standalone pv applications with a hybrid energy storage system, *Energies* 12 (5) (2019) 902.
- [26] P. Singh, J. Lather, Artificial neural network-based dynamic power management of a dc microgrid: a hardware-in-loop real-time verification, *International Journal of Ambient Energy* (2020) 1–9.
- [27] V. Herrera, A. Milo, H. Gaztañaga, I. Etxeberria-Otadui, I. Villarreal, H. Camblong, Adaptive energy management strategy and optimal sizing applied on a battery-supercapacitor based tramway, *Applied Energy* 169 (2016) 831–845.
- [28] L. W. Chong, Y. W. Wong, R. K. Rajkumar, D. Isa, An optimal control strategy for standalone pv system with battery-supercapacitor hybrid energy storage system, *Journal of Power Sources* 331 (2016) 553–565.
- [29] B. Xu, J. Shi, S. Li, H. Li, Z. Wang, Energy consumption and battery aging minimization using a q-learning strategy for a battery/ultracapacitor electric vehicle, *Energy* 229 (2021) 120705.
- [30] International Energy Agency, Technology mix in storage installations excluding pumped hydro, 2011-2016 [Online], Available: <https://www.iea.org/data-and-statistics/charts/technology-mix-in-storage-installations-excluding-pumped-hydro-2011-2016> (Accessed: Aug. 06, 2021).
- [31] International Energy Agency, Energy Storage [Online], Available: <https://www.iea.org/reports/energy-storage> (Accessed: Aug. 06, 2021).
- [32] A. Pesaran, S. Santhanagopalan, G. Kim, Addressing the impact of temperature extremes on large format li-ion batteries for vehicle applications (presentation), Tech. rep., National Renewable Energy Lab.(NREL), Golden, CO (United States) (2013).
- [33] R. Hutchinson, Temperature effects on sealed lead acid batteries and charging techniques to prolong cycle life., Tech. rep., Sandia National Laboratories (2004).
- [34] G. Albright, J. Edie, S. Al-Hallaj, A comparison of lead acid to lithium-ion in stationary storage applications, Published by AllCell Technologies LLC, 2012.
- [35] F. Leng, C. M. Tan, M. Pecht, Effect of temperature on the aging rate of li ion battery operating above room temperature, *Scientific reports* 5 (2015) 12967.
- [36] Z. Song, H. Hofmann, J. Li, J. Hou, X. Zhang, M. Ouyang, The optimization of a hybrid energy storage system at subzero temperatures: Energy management strategy design and battery heating requirement analysis, *Applied Energy* 159 (2015) 576–588.
- [37] W. Yang, F. Zhou, H. Zhou, Y. Liu, Thermal performance of axial air cooling system with bionic surface structure for cylindrical lithium-ion battery module, *International Journal of Heat and Mass Transfer* 161 (2020) 120307.

- [38] S. S. Katoch, M. Eswaramoorthy, A detailed review on electric vehicles battery thermal management system, in: IOP Conference Series: Materials Science and Engineering, Vol. 912, IOP Publishing, 2020, p. 042005.
- [39] J. Li, Z. Zhu, Battery thermal management systems of electric vehicles, Master's thesis, Chalmers University of Technology (2014).
- [40] Z. Qu, Z. Jiang, Q. Wang, Experimental study on pulse self-heating of lithium-ion battery at low temperature, *International Journal of Heat and Mass Transfer* 135 (2019) 696–705.
- [41] D. Shin, M. Poncino, E. Macii, Thermal management of batteries using supercapacitor hybrid architecture with idle period insertion strategy, *IEEE Transactions on Very Large Scale Integration (VLSI) Systems* 26 (6) (2018) 1159–1170.
- [42] R. de Castro, R. E. Araujo, Model predictive power allocation for hybrid battery balancing systems, in: 2019 IEEE Vehicle Power and Propulsion Conference (VPPC), IEEE, 2019, pp. 1–5.
- [43] Z. Huang, Y. Le, H. Liao, Y. Zhou, Y. Wu, H. Li, S. Li, X. Lu, J. Peng, A temperature-suppression power allocation strategy for hybrid energy management of evs, in: 2019 IEEE Energy Conversion Congress and Exposition (ECCE), IEEE, pp. 3542–3547.
- [44] D.-A. Ciupageanu, L. Barelli, G. Lazaroiu, Real-time stochastic power management strategies in hybrid renewable energy systems: A review of key applications and perspectives, *Electric Power Systems Research* 187 (2020) 106497.
- [45] D.-A. Ciupageanu, L. Barelli, G. Lazaroiu, Design of a fuzzy logic controller for a remote power application, in: 2019 IEEE PES Innovative Smart Grid Technologies Europe (ISGT-Europe), IEEE, 2019, pp. 1–5.
- [46] X. Lü, Y. Wu, J. Lian, Y. Zhang, Energy management and optimization of pemfc/battery mobile robot based on hybrid rule strategy and ampso, *Renewable Energy* 171 (2021) 881–901.
- [47] T. J. Ross, *Fuzzy Logic with Engineering Applications*, 4th Edition, John Wiley & Sons, Ltd, Southern Gate, Chichester, West Sussex, United Kingdom, 2017.
- [48] O. Cordón, F. Herrera, F. Hoffmann, L. Magdalena, *Genetic Fuzzy Systems*, World Scientific Publishing Co. Pte. Ltd, 2001.
- [49] MathWorks [®], *Fuzzy logic toolbox™: User's guide* (2019).
- [50] P. Sanchis, A. Ursæa, E. Gubía, L. Marroyo, Boost dc-ac inverter: a new control strategy, *IEEE Transactions on power electronics* 20 (2) (2005) 343–353.
- [51] MathWorks [®], *Global Optimization Toolbox: User's guide* (2019).
- [52] A. Majumdar, *Soft Computing in Textile Engineering*, Elsevier, Philadelphia, PA, 2010.
- [53] A. Meyer-Baese, V. J. Schmid, *Pattern Recognition and Signal Analysis in Medical Imaging*, Elsevier, San Diego, CA, 2014.
- [54] Lygte-info, Battery test for small batteries, comparator [Online], Available: <https://lygte-info.dk/review/batteries2012/CommonSmallcomparator.php> (Accessed: Feb. 04, 2021).
- [55] Maxwell [®] Technologies, Supercapacitor datasheet [Online], Available: <https://www.maxwell.com/products/ultracapacitors/download> (Accessed: Feb. 04, 2021).
- [56] D. A. Schoenwald, S. R. Ferreira, D. M. Rosewater, D. R. Conover, A. Crawford, J. Fuller, S. Gourisetti, V. Viswanathan, Protocol for uniformly measuring and expressing the performance of energy storage systems., Tech. rep., Sandia National Lab.(SNL-NM), Albuquerque, NM (United States) (2016).
- [57] J. Wang, P. Liu, J. Hicks-Garner, E. Sherman, S. Soukiazian, M. Verbrugge, H. Tataria, J. Musser, P. Finamore, Cycle-life model for graphite-lifepo4 cells, *Journal of power sources* 196 (8) (2011) 3942–3948.

- [58] E. Redondo-Iglesias, P. Venet, S. Pelissier, Eyring acceleration model for predicting calendar ageing of lithium-ion batteries, *Journal of Energy Storage* 13 (2017) 176–183.